A Novel Impervious Surface Extraction Method Based on Automatically Generating Training Samples From Multisource Remote Sensing Products: A Case Study of Wuhan City, China

Yingbing Liu, Yuqin Wu, Zeqiang Chen, Min Huang, Wenying Du, Nengcheng Chen, and Changjiang Xiao

***Abstract*—Impervious surfaces caused by rapid urbanization affect the environment and increase the disaster risk. Currently, most articles have extracted impervious surfaces by manual participation for training samples with medium-and-high spatial resolution remote sensing images. Therefore, it is necessary to develop a new method for improving the efficiency of training sample acquisition and the accuracy of impervious surface extraction. In this article, a novel impervious surface extraction method is proposed based on automatically generating training samples from multisource remote sensing products. First, the preliminary sample area was constructed through the overlay analysis of the classification consistency area of three remote sensing products and homogeneous area detection based on Sentinel-2 images. Second, four spectral indices and digital surface model (DSM) elevation data were used for sample selection, and the pixels were further purified by variance purification calculation. Finally, by sample migration and random forest model training, impervious surfaces were extracted for other years with limited data. Wuhan city in China was selected as the study area due to a large number of interior objects for impervious surfaces. Sentinel-2 images from 2018 to 2020, three 30 m-resolution products, and DSM data in 2018 were used. The proposed method's extraction accuracies of impervious surfaces for Wuhan in 2018, 2019, and 2020 are 94.02%, 94.45%, and 93.87%, respectively. Additionally, with the resolution improved up to 10 m, the method is more conducive to distinguishing the boundary between impervious surfaces and pervious surfaces.**

***Index Terms*—Automatically generating training samples, impervious surface extraction, random forest, remote sensing products, training sample migration.**

Manuscript received 5 March 2022; revised 7 May 2022, 16 June 2022, and 10 July 2022; accepted 6 August 2022. Date of publication 10 August 2022; date of current version 26 August 2022. This work was supported in part by the National Key R&D Program under Grant 2018YFB2100500; in part by the National Nature Science Foundation of China Program under Grant 42001372, Grant 41971351, and Grant 41771422; in part by the project funded by the China Postdoctoral Science Foundation under Grant 2019M661621 and Grant 2021T140513; in part by the Open Fund of National Engineering Research Center for Geographic Information System, China University of Geosciences under Grant 2021KFJJ07; in part by the Shanghai Municipal Science and Technology Major Project under Grant 2021SHZDZX0100; and in part by the Shanghai Municipal Commission of Science and Technology Project under Grant 19511132101. *(Corresponding author: Changjiang Xiao.)*

Yingbing Liu is with the School of Computer Science and Technology, Hainan University, Haikou 570228, China (e-mail: ybingliu@hainanu.edu.cn).

Yuqin Wu is with the Zhongnan Engineering Corporation Limited, Power China, Changsha 410014, China (e-mail: wuyq2019@whu.edu.cn).

Zeqiang Chen and Nengcheng Chen are with the National Engineering Research Center for Geographic Information System, China University of Geosciences, Wuhan 430078, China, and also with the State Key Laboratory for Information Engineering in Surveying, Mapping and Remote Sensing, Wuhan University, Wuhan 430079, China (e-mail: chenzeqiang@cug.edu.cn; chennengcheng@cug.edu.cn).

Min Huang is with the School of Geography and Environment, Jiangxi Normal University, Nanchang 330027, China (e-mail: minhuang@whu.edu.cn).

Wenying Du is with the National Engineering Research Center for Geographic Information System, China University of Geosciences, Wuhan 430078, China (e-mail: duwenying@cug.edu.cn).

Changjiang Xiao is with the College of Surveying and Geo-Informatics, Tongji University, Shanghai 200092, China, and also with the Frontiers Science Center for Intelligent Autonomous Systems, Shanghai 201210, China (e-mail: cjxiao@tongji.edu.cn).

Digital Object Identifier 10.1109/JSTARS.2022.3197760

I. Introduction

IMPERVIOUS surfaces can prevent the infiltration of water into the soil, which is always accompanied by ground hardening, affects the green ecological environment of urban areas, aggravates urban heat islands and nonpoint source pollutants, and increases the risk, intensity, and duration of urban waterlogging with a heavy burden on drainage facilities [1], [2], [3], [4], [5], [6]. Efficient extraction and accurate estimation of impervious surfaces are of great significance for urban planning, environmental assessment, and ecological protection. Due to the rapid development of remote sensing technology, remote sensing images with an easy acquisition, wide coverage, high efficiency, and diverse data have been the main means of extracting impervious surfaces.

Impervious surface extraction is a subset of remote sensing image classification utilizing techniques, such as spectral mixture analysis [7], [8], [9], index method [10], [11], [12], regression model [13], [14], [15], decision trees [16], [17], random forest [18], [19], [20], [21], and deep learning [22], [23], [24], [25]. Among them, the extraction accuracy of impervious surfaces through spectral mixture analysis is limited by the large differences between endmember spectra and actual images. Especially, when obtaining manual endmembers from

image analysis, it is difficult to select good training samples for the mixed pixels classification [26], which is not conducive to automatic and rapid extraction of impervious surfaces. The index method is based on the spectral index, which is used to distinguish whether a pixel belongs to the impervious surface according to the value of the corresponding index. It adopts the form of combining multiple indices or using the index of impervious surfaces as auxiliary data for sample extraction and other classification methods. The regression model is greatly affected by the time of image acquisition. Meanwhile, the representative methods of sample selection and the minimal number of necessary samples are important to improve the efficiency of the regression model [27]. Decision trees usually need train samples and add original image bands and spectral indices as new bands to establish classification rules. The small number of training samples might lead to the loss of important information, and the classification rules could not be well explained, but a large number of training samples could lead to the increase of the nodes for the decision tree and interfere with its accuracy [28]. Random forest [29], [30] can achieve reasonable results even without hyperparameter adjustment, and the relative importance of each feature in the prediction process can be easily measured, which is simple and flexible to use. Although the random forest classifier is sensitive to the sampling design, it has been proven to be suitable for classifying hyperspectral data [31], [32]. Deep learning can integrate various features of remote sensing images, but it relies on using a complex model with poor interpretability, high hardware requirements, and many training samples. In particular, the number and diversity of training samples are essential to the multilayer neural networks of deep learning [33].

The selection of training samples for impervious surfaces is mainly based on manual participation in the labor-intensive and time-consuming task, which requires strong prior knowledge and cannot be efficiently applied to automatic impervious surface extraction [34], [35]. Some articles have also trained samples in a semiautomatic manner by computing-related impervious surface indices or integrating ancillary data products while demarcating training samples manually [36], [37], [38]. Additionally, some articles have focused on threshold detection, saliency analysis, and building indices from various remote sensing images for automatic sample extraction, but their practicalities are relatively insufficient and are constrained by the features of objects and pixels, and indices of impervious surfaces. Wang and Li [39] proposed an urban impervious surface automatic threshold detection model from multitemporal Landsat images to reduce manual interference for threshold fine-tuning and reselection, which depends on the capability of the urban impervious surface index to express or depict different land cover types. Tan et al. [40] used two groups of threshold ranges instead of one threshold to obtain more evenly distributed training samples with the parameter values settled empirically through trial and error. Hou et al. [41] designed a saliency-guided edge-preservation framework for semiautomatically updating building databases with limited manual annotation. Zhou et al. [42] developed an automatic sample extraction strategy for both no-change and change samples; however, the strategy is not suitable for impervious surfaces containing high-rise buildings, and it is difficult to determine the parameters for samples with different feature types. Sebari and He [43] proposed an automatic determination of the brightness index threshold based on the histogram frequencies of images to define the discriminative thresholds, but it may confuse some objects presenting the same spectral responses. Liu et al. [44] proposed an automated extraction method of built-up areas to represent the vertical properties of buildings based on multiview images, but it leads to errors from similar features.

Previous articles on remote sensing products of impervious surfaces and land use have mostly used remote sensing images with medium-and-high spatial resolution. Specifically, many products are at medium resolution (10–100 m) with time series, but few are at high resolution ($<$10 m) with temporal updates [45]. Considering the requirements of refined urban construction and management, the existing numerous remote sensing products, such as the 500-m resolution MODIS data in 2000 [46], 300-m resolution global land cover and land cover change for each year from 1992 to 2015 [47], 30-m resolution Global Human Settlement Built-Area data in 1975, 1990, 2000, and 2014 [48], 30-m resolution finer resolution observation and monitoring of the global land cover (FROM-GLC) in 2010 and 2015 and 10-m resolution FROM-GLC in 2017 [49], [50], 30-m resolution global urban land impervious surface product from 1990 to 2015 with a 5-year interval [51], [52], 30-m resolution GlobeLand30 in 2000 and 2010 [53], 30-m resolution annual China land cover dataset from 1990 to 2019 [54], 10-m resolution Environmental Systems Research Institute (ESRI) 2020 global land use land cover (LULC) for each year from 2017 to 2021 [55], [56], 10-m resolution European Space Agency (ESA) WorldCover in 2020 [57], and 2-m resolution impervious surface in mainland China in 2017 [58], cannot completely satisfy the needs of spatiotemporal refinement in recent years. The production process of training samples for existing impervious surface products mostly requires manual intervention, which increases the workload and reduces efficiency. In addition, due to the various feature types of ground objects for impervious surfaces, the composition of the urban landscape is complex, especially in areas where different ground objects are mixed. The mixed pixel problem of high-resolution remote sensing images greatly affects the classification results of extracting impervious surfaces, and small ground objects such as houses and roads have a high probability of being wrongly classified [4], [59], [60], [61]. Therefore, an important problem that urgently needs to be solved is how to automatically generating training samples from medium-and-high resolution remote sensing images and products to reduce repetitive manual participation in sample acquisition and improve the efficiency of impervious surface extraction.

To solve the abovementioned problems, this article proposed a novel impervious surface extraction method based on automatically generating training samples from multisource remote sensing products. The goals of this article include the following: 1) propose a method that can automatically generate training samples with several feature types of ground objects; 2) extract impervious surfaces with higher spatial resolution in different

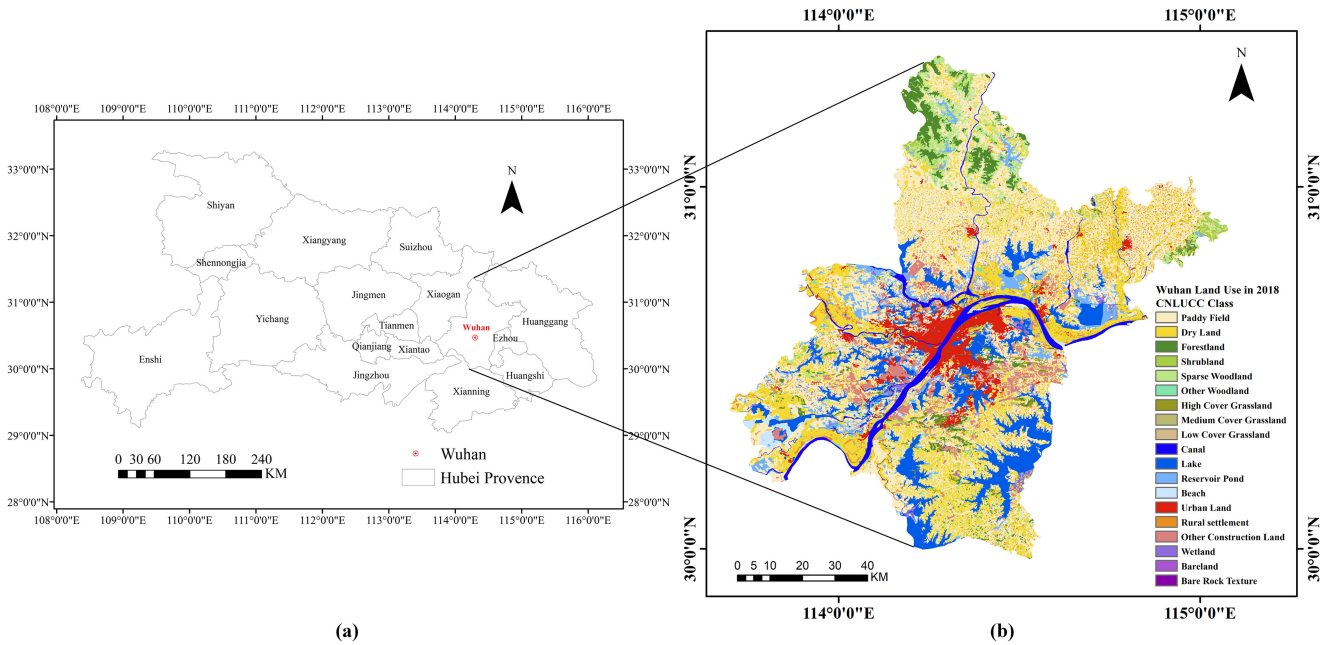

Fig. 1. Location of the study area. (a) Wuhan city in Hubei Province of China. (b) Spatial distribution of land use types from China's multiperiod land use land cover remote sensing monitoring data set (CNLUCC) of Wuhan in 2018.

years based on a certain limited year and evaluate the classification accuracy; and 3) investigate the feasibility, effectiveness, and advantages of the method proposed for the automatic extraction of impervious surfaces.

II. Study Area and Data

A. Study Area

The study area is Wuhan city, which is located in Hubei Province of China with a geographical location of 113°41′E to 115°05′E and 29°58′N to 31°22′N and covers an area of approximately 8569.15 km^2. It is an economically developed region with a high level of urbanization and rapid urban development. There are various types of interior objects in Wuhan with obvious urban boundaries, which form a concentrated and wide distribution of impervious surfaces. Therefore, automatic extraction of training samples and accurate estimation of impervious surfaces in Wuhan are of vital importance to urban planning, spatial coordination, and environmental protection, but they have rarely been investigated in previous article. In this article, the location of the study area and the spatial distribution of land use types from China's multiperiod LULC remote sensing monitoring dataset (CNLUCC) [62] of Wuhan in 2018 are shown in Fig. 1. The urban land, rural settlement, and other construction land are the typical types of impervious surfaces in CNLUCC.

B. Data

1) Products and Preprocessing: The data used in this article mainly include the Sentinel-2 Level-1C product from the ESA [63], global artificial impervious area (GAIA) from Tsinghua University [64], [65], [66], [67], annual urban land maps (AULM) from Liu et al. [68], CNLUCC from the Resource and Environment Science and Data Center of the Chinese Academy of Sciences, and Advanced Land Observing Satellite (ALOS) World 3-D-30 m (AW3D30) version 2.1 product of the global digital surface model (DSM) from the Japan Aerospace Exploration Agency (JAXA) [69]. The seasonal data with strong vegetation growth from June 1 to October 31 are composited to Sentinel-2 image bands by spectral indices to reduce the interference of bare soil for impervious surfaces. The type, spatial resolution, and time coverage of the multisource remote sensing products used in this article are shown in Table I. In addition, the bands and parameters of Sentinel-2 images can be obtained in detail from the Earth Observing System website (https://eos.com/find-satellite/sentinel-2/). The vector data used in this article come from the boundary data of China's counties and cities, including the administrative boundary of Wuhan, and it is mainly used for image cropping.

Sentinel-2 image preprocessing is performed through the Google Earth Engine, including the cloud removal using QA60 band with cloud mask information and the atmospheric correction. For the classification system of products, similar to the GAIA and AULM, which both include two types of impervious surfaces and pervious surfaces, it is necessary to reclassify CNLUCC with six first-level types into two types. The five types of arable land, woodland, grassland, waters, and unused land are reclassified into pervious surfaces, while the type of urban and rural, residential, industrial, and mining land is reclassified into impervious surfaces. The grids representing impervious surfaces and pervious surfaces in the three remote sensing products are assigned values of 1 and 0, respectively, to maintain data consistency.

2) Validation Sample Set: Based on the high-resolution images on the Google Earth platform, the verification sample sets of Sentinel-2 images in Wuhan contain 1671 samples (410

TABLE I
MULTISOURCE REMOTE SENSING PRODUCTS WERE USED IN THIS ARTICLE

Type	Product	Spatial resolution	Time coverage
Remote sensing image	Sentinel-2 Level-1C	10 m	June 1 to October 31 for each year from 2018 to 2020
	GAIA		
Classification product	AULM	30 m	2018
	CNLUCC		
Digital surface model	AW3D30 Version2.1	30 m	2006-2011

impervious surface samples and 1261 pervious surface samples) in 2018, 1622 samples (279 impervious surface samples and 1343 pervious surface samples) in 2019, and 1632 samples (289 impervious surface samples and 1343 pervious surface samples) in 2020, which are marked through visual interpretation. To better evaluate the performance of the classification results, the number of impervious surfaces in the validation sample set is relatively large, the numbers of arable land, woodland, and grassland are moderate, the number of easily distinguishable water bodies is small, and unused land with a small total area is the smallest. In addition, due to the large difference in the size and area of a single object for different ground features, all samples are selected to maintain the same size.

III. METHODOLOGY

The proposed impervious surface extraction method based on automatically generating training samples from multisource remote sensing products is presented in Fig. 2. First, a preliminary sample area based on the classification consistency area of remote sensing products and homogeneous area detection of Sentinel-2 images is constructed with impervious surfaces and pervious surfaces. Second, spectral index selection and variance purification calculation are used to improve the data processing efficiency and sample quality after sample overlay analysis. A training sample set containing six types of feature types for ground objects is generated. Third, based on the generated training samples in a certain year with available classification products, the training samples in other years with limited classification products are generated by training sample migration. Finally, the impervious surfaces in a certain year and other years are extracted by random forest model training.

A. Preliminary Sample Area Construction

1) Classification Consistency Area: To comprehensively consider the consistency and difference of multisource remote sensing products, overlay analysis is used to objectively combine the classification results of GAIA, AULM, and CNLUCC. The classification consistency area is regarded as the true value of the classification result. For the overlay analysis, the original images used by GAIA, AULM, and CNLUCC are all Landsat, and the raster position is the same. By using raster overlay calculation to extract the three products with the same value, we further set the impervious surface grid value to 1 and the pervious surface grid value to 0; that is, the classification consistency area of the existing products can be obtained. Fig. 3 shows the distribution of the classification consistency area of the three products for GAIA, AULM, and CNLUCC of Wuhan in 2018. The red and blue areas in Fig. 3 represent the consistent areas that are classified as impervious surfaces and pervious surfaces for all three products, respectively, which are suitable for scenarios where the types of features are relatively singular and there is a wide distribution of certain features.

By comparing the number of grids with the three areas, more than 80% of the grids have consistent classification results, indicating that the classification results of the three products have relatively small differences. In addition, the yellow area in Fig. 3 indicates the area where the classification results of the three products are inconsistent, which are mostly in areas where populations and buildings are densely populated with other surrounding features. The feature types in the inconsistent classification area are complex and need to be further extracted to improve the classification accuracy of impervious surfaces.

2) Homogeneous Area Detection: To improve the classification accuracy of impervious surfaces, four spectral indices, the normalized difference vegetation index (NDVI) [70], modified normalized difference water index (MNDWI) [71], normalized difference building index (NDBI) [72], and soil extraction index (SoEI) [73], are calculated by the original bands of the Sentinel-2 image. The annual maximum NDVI is used to reflect the surface vegetation density and plant growth. The annual median MNDWI can improve the effectiveness of water extraction, and is beneficial to the case of many buildings in urban areas. The annual minimum NDBI is usually used to extract the urban building land, in particular, to distinguish the spectral characteristics between buildings and bare land. The annual median SoEI is used as the basis for classifying bare soil to distinguish bare soil and impervious surfaces. The elevation of DSM data is also fused to the band of the Sentinel-2 image to provide ground object elevation information of urban buildings and vegetation. Therefore, adding the 13 bands of the original Sentinel-2 image, the composite Sentinel-2 image contains a total of 18 bands.

The ISODATA algorithm is used for the unsupervised classification of the composite Sentinel-2 image, which is divided into n-by-n pixel blocks through cluster analysis. The areas where the pixels in the block of n-by-n pixels are all divided into one type are regarded as homogeneous areas. The spatial resolution of the Sentinel-2 image is 10 m, while the three remote sensing products of GAIA, AULM, and CNLUCC are all 30 m. Therefore, one product grid of GAIA, AULM, or CNLUCC corresponds to 3-by-3 Sentinel-2 image pixels. To avoid mixed pixels with different feature types in the Sentinel-2

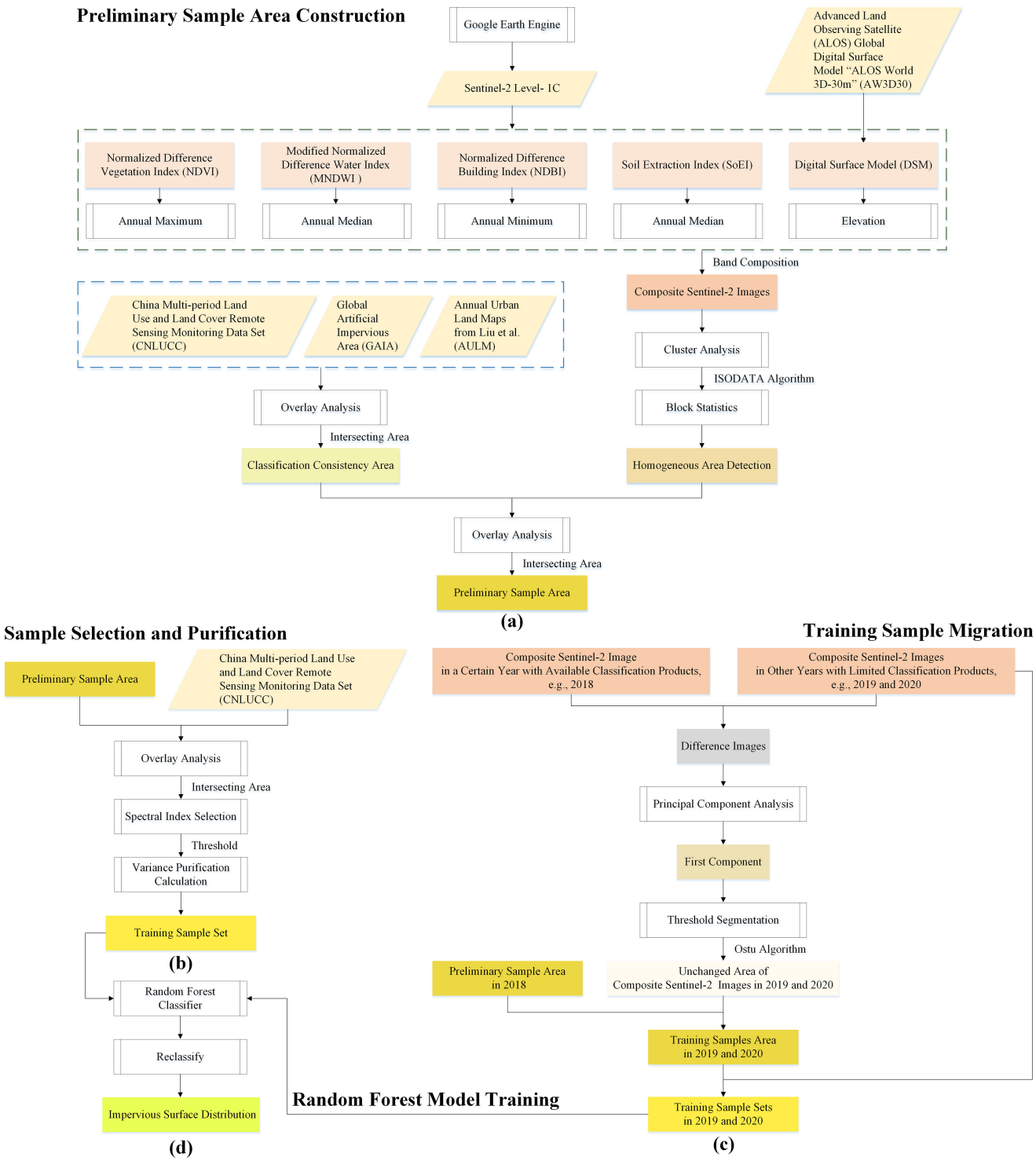

Fig. 2. Workflow of the proposed impervious surface extraction method based on automatically generating training samples from multisource remote sensing products.

image for the sample area in the product grid, it can be judged by calculating whether the 3-by-3 Sentinel-2 image pixels in each product grid belong to the same type. The 3-by-3 Sentinel-2 image pixels contained in the 30 m-by-30 m product grid include two cases (Fig. 4): 1) the nine pixels are of the same type and 2) the nine pixels are not of the same type. For the detection of the homogeneous area for the 10-m resolution Sentinel-2 image with the 30-m resolution remote sensing products, the area that meets the first situation is regarded as a homogenous area that can be ultimately retained; otherwise, it is regarded as a nonhomogeneous area that should be removed.

Homogeneous area detection can be achieved by the Block Statistics method of the spatial analyst in the ArcGIS software [74]. The type of block is set to a 3-by-3 rectangle to calculate the

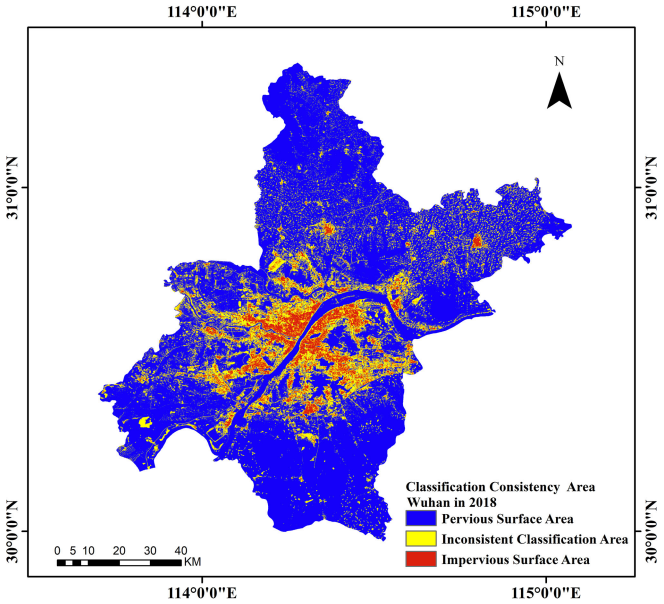

Fig. 3. Distribution map of the classification consistency area of the three remote sensing products for GAIA, AULM, and CNLUCC of Wuhan in 2018.

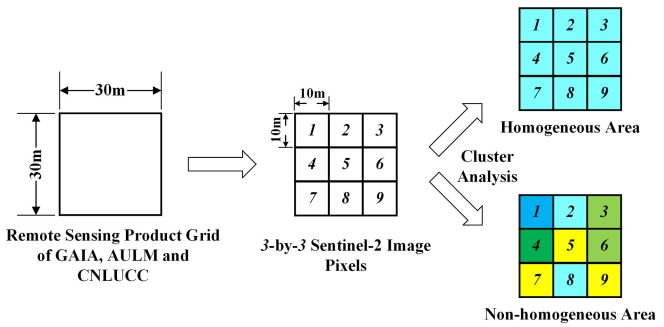

Fig. 4. Schematic diagram of the homogeneous area detection for the 10-m resolution Sentinel-2 image with 30-m resolution remote sensing products. Different colors represent diverse feature types within the block of 3-by-3 Sentinel-2 image pixels.

number of feature types contained in each block in the Sentinel-2 image classification result. The composite Sentinel-2 image of Wuhan in 2018 is calculated by the Block Statistics method, and the pixels with a value of 1 are the homogeneous area to be extracted (Fig. 5). The pixel proportion of the homogenous area is 94.39% of the total pixel number of the composite Sentinel-2 image of Wuhan in 2018, accounting for the majority. Homogeneous areas are generally distributed in the internal area of a single object, especially in areas such as arable land and waters that are widely distributed and occupy a large area, with the pixels forming a large continuous area. In densely populated urban areas and rural areas, the distribution of homogeneous area pixels is significantly more scattered.

B. Sample Selection and Purification

1) Preliminary Sample Overlay Analysis: Through the overlay analysis of the classification consistency area of the remote sensing products and the homogeneous area of the composite

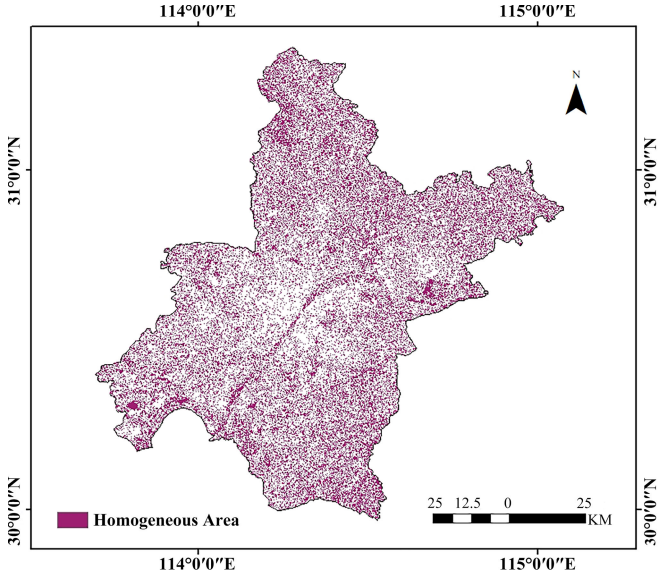

Fig. 5. Distribution map of the homogeneous area for the composite Sentinel-2 image of Wuhan in 2018.

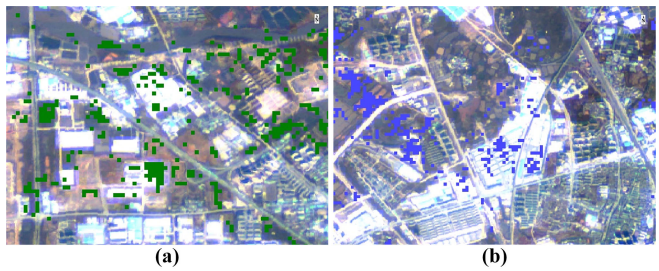

Fig. 6. Some samples with incorrect types are in the preliminary sample area. (a) Incorrect arable land samples. (b) Incorrect water samples.

Sentinel-2 image, the intersecting area is the required preliminary sample area. However, the preliminary sample area is still large, and there are some samples with incorrect types that are not consistent with the actual feature types (Fig. 6). Therefore, to further refine the selection of training samples, the preliminary sample area with two types of impervious surfaces and pervious surfaces is analyzed overlapping with the CNLUCC with six feature types.

Through the overlay analysis of the preliminary sample area and the CNLUCC, the type code values of six feature types in CNLUCC are assigned to the corresponding pixels in the same location of the preliminary sample area. The type code values are 1 to 6, corresponding to the first level of CNLUCC (Table II). Among them, the original impervious surface corresponds to CNLUCC type code 5, that is, urban and rural, residential, industrial, and mining land. The original pervious surface corresponds to the other five CNLUCC type codes.

2) Spectral Index Selection: To further improve the accuracy of the training samples, the overlapped pixels in the preliminary sample area are selected and purified by spectral indices. Four spectral indices, NDVI, MNDWI, NDBI, and SoEI, are used to set thresholds to exclude samples with obvious misclassification. According to the field investigation and image comparison, the

TABLE II
TYPE CODES OF PRELIMINARY SAMPLES AFTER OVERLAY ANALYSIS WITH CNLUCC

Original sample types	CNLUCC feature types	Type codes
Pervious surface	Arable land	1
	Woodland	2
	Grassland	3
	Waters	4
	Unused land	6
Impervious surface	Urban and rural, residential, industrial, and mining land	5

TABLE III
THRESHOLDS USED IN SPECTRAL INDICES CORRESPONDING TO SIX FEATURE TYPES FOR SAMPLE SELECTION

Spectral indices	Feature type code					
	1	2	3	4	6	5
NDVI		> 0.4	> 0.4			
MNDWI				> 0.1		< 0.45
NDBI	< -0.1				> -0.35	< 0.1
SoEI	> 0.5					

selection thresholds of the four spectral indices are shown in Table III. For all image pixels in the preliminary sample area, based on the specific feature type to determine whether the corresponding spectral index meets the filtering threshold conditions, the pixels that do not meet the conditions are removed from the training sample set.

3) Variance Purification Calculation: After the filtering of spectral index selection, the number of remaining samples is still large and needs to be further purified. The method of variance purification [75], [76], [77] can remove pixels with large deviations from the average value and eliminate incorrect samples. The calculation process of variance purification was as follows:

Step 1: Build the average spectral vector $(\overline{x_i})$, $i = 1, 2, 3, \ldots, n$ of the training samples for each feature type in the study area, x_i is the spectral vector, and n is the size of the training samples built from spectral index selection.

Step 2: Calculate the variance $\mathrm{Var}(x_i)$ between the spectral vector x_i by each pixel for each feature type and the corresponding average spectral vector $(\overline{x_i})$, as in

$$\mathrm{Var}\,(x_i) = \sum_{i=1}^{n} (x_i - \overline{x_i})^2. \tag{1}$$

Step 3: Calculate the average of the variances $\mathrm{aveVar}(x_i)$.

Step 4: Judge each pixel for each feature type to remove impure pixels. If the variance $\mathrm{Var}(x_i)$ of the spectral vector of a pixel is greater than A times the average of the variances $\mathrm{aveVar}(x_i)$, the pixel can be considered impure. The purified samples p_i are calculated as in (2). A is the coefficient that depends on the specific situation to ensure sufficient samples

$$p_i = \begin{cases} x_i,\ if\ Var\,(x_i) \le A \times aveVar\,(x_i) \\ None,\ if\ Var\,(x_i) > A \times aveVar\,(x_i) \end{cases}$$
$$i = 1, 2, 3, \ldots, n. \tag{2}$$

Step 5: Extract the purified training sample set of $\{p_i\}$, $i = 1, 2, 3, \ldots, m$, where m is the size of purified training samples.

For the average spectral vector, four spectral indices and DSM elevation are merged into the bands of the sentinel-2 image. It is necessary to normalize the samples with all 18 bands of the composite Sentinel-2 image and calculate the average spectral vector and variance. Considering the characteristics of ground objects, different coefficients A of the six feature types are set separately. The urban and rural, residential, industrial, and mining land for impervious surfaces is often easily confused with arable land. Additionally, given the training sample sizes of feature types, the coefficients A of the urban and rural, residential, industrial, and mining land and the arable land are set to 3.5 and 3, respectively, to improve their classification accuracy. The feature types of woodland, grassland, waters, and unused land have obvious characteristics with small gaps, and their coefficients A are all set to 1.5. The training sample set containing six feature types of Wuhan in 2018 is obtained with automated extraction to reduce repetitive manual participation. The quantity and proportion of the six feature types for training samples before and after sample selection and purification are shown in Table IV.

C. Training Sample Migration

Due to the limited coverage time of the remote sensing products of GAIA, AULM, and CNLUCC, only the training samples of Wuhan in 2018 are obtained. However, considering that the actual features may change in different years, the training samples in 2018 cannot be directly used to extract the impervious surfaces in other years. Therefore, to use the constructed training sample set in 2018 for impervious surface extraction over a longer period, the training sample migration method is adopted to extract the training sample sets of Sentinel-2 images of Wuhan in 2019 and 2020. For the composite Sentinel-2 images of Wuhan in 2019 and 2020, the change detection method based on principle component analysis is used to retain the unchanged areas in the sample area. Through overlay analysis, the unchanged areas in 2019 and 2020 are superimposed with the sample area in 2018 to generate the training sample set for the corresponding year.

The specific process of training sample migration is shown in Fig. 2(c). For the other years with limited classification products of impervious pervious or land use (e.g., Wuhan in 2019 and 2020), the composite Sentinel-2 images of this year and a certain year with available classification products (e.g., Wuhan in 2018) are subtracted pixel by pixel and band by band, and the absolute values of the difference images are taken. The main difference information between the difference images is concentrated in

TABLE IV
COMPARISON OF THE QUANTITY AND PROPORTION OF THE SIX FEATURE TYPES FOR THE TRAINING SAMPLES OF WUHAN IN 2018 BEFORE AND AFTER SAMPLE SELECTION AND PURIFICATION

	Sample selection and purification			
	Before		After	
Reclassification types	Quantity (pixels)	Proportion (%)	Quantity (pixels)	Proportion (%)
Arable land	17630678	60.11	12480383	69.64
Woodland	3879665	13.22	2607137	14.54
Grassland	276964	0.94	200683	1.12
Waters	6605909	22.52	1805802	10.08
Urban and rural, residential, industrial, and mining land	691173	2.36	660428	3.69
Unused land	246451	0.84	167255	0.93
Total	29330840		17921688	

the first component of the principle component. The Otsu algorithm is used to obtain the segmentation threshold of the first component image, and the image is divided into unchanged and changed areas after binarization. The changed area is removed from the training sample area, and only the overlapping part of the sample area and the pixels of the image in the unchanged area remain as the training samples of the year required. Based on the generated training samples of Wuhan in 2018, the training samples of Wuhan in 2019 and 2020 are obtained according to the training sample migration, respectively.

D. Random Forest Model Training

The random forest model has advantages for large and high-dimensional data classification; thus, it is selected as the classifier for impervious surface automatic extraction. The input data of random forest model training come from the training samples containing six feature types of Wuhan from 2018 to 2020. Since the input training samples have six feature types, the output classification results also contain the same types. Therefore, the five feature types of arable land, woodland, grassland, waters, and unused land are further reclassified as pervious surfaces, and the one feature type of urban and rural, residential, industrial, and mining land is reclassified as impervious surfaces.

Through the stratified sampling method, 5000 samples of each feature type are selected each year as the training samples of the random forest model. By adding the label of the feature type to each sample, the spectral data of the composite Sentinel-2 images are used as the classification features with a total of 18 features, including the 13 original bands and the added NDVI, MNDWI, NDBI, and SoEI indices and DSM elevation data. The classification features are set as each band of the input image, and the default setting is the square of the total number of features. The feature importance normalization parameters can be returned with total values of 1 through the random forest classifier, which can represent the importance of each feature.

The normalized values of the importance of band features for the composite Sentinel-2 images by random forest model training are shown in Fig. 7. The larger the normalized value is, the greater the importance of the band feature. Among the 18 bands, the B1 (coastal aerosol), B2 (blue), B9 (water vapor), and DSM bands are of higher importance, while the band importance

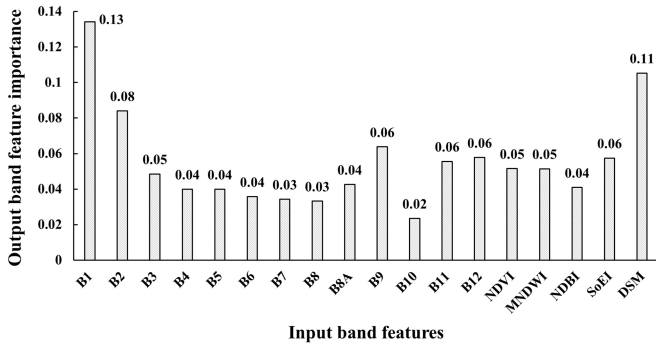

Fig. 7. Normalized values of the importance of band feature for the composite Sentinel-2 images by random forest model training.

of B6 (vegetation red edge), B7 (vegetation red edge), B8 (NIR), and B10 (SWIR-Cirrus) is relatively low.

IV. RESULTS AND DISCUSSION

A. Results

1) Impervious Surface Mapping Results: The final results of the impervious surface distribution in Wuhan from 2018 to 2020 are shown in Fig. 8. The blue areas in Fig. 8 represent the impervious surfaces, which demonstrate the feasibility of automatically generating training samples based on existing multisource remote sensing products.

Based on the established validation sample set, the accuracy of the extraction results of the impervious surface distribution in Wuhan from 2018 to 2020 is evaluated (Table V) by the confusion matrix with the overall accuracy (OA), kappa coefficient, user's accuracy (UA), and production's accuracy (PA). With the classification results in this article, the extraction accuracies of impervious surfaces for Wuhan in 2018, 2019, and 2020 were 94.02%, 94.45%, and 93.87%, respectively. This shows that the training samples obtained by the method proposed in this article have high accuracy, and the classification of impervious surfaces performs well. Thus, the training sample sets of impervious surfaces in existing years generated according to the method proposed can be used for Sentinel-2 images or other high-resolution images in other years by training sample migration for long-term series of impervious surface extraction.

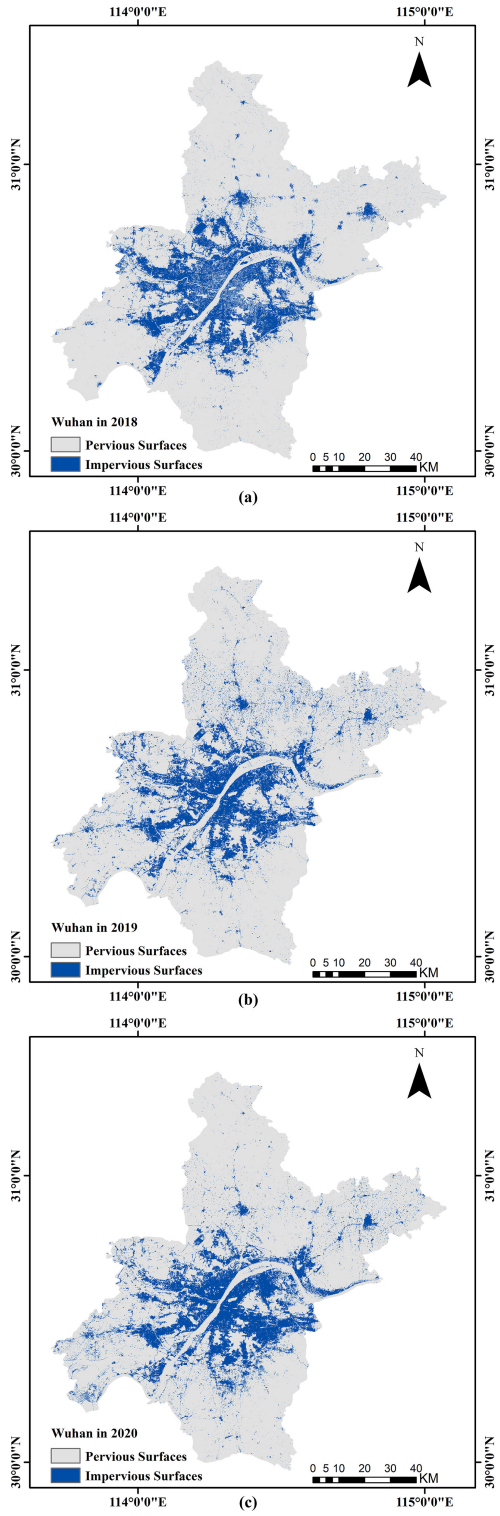

Fig. 8. Distribution of impervious surfaces extracted in Wuhan from 2018 to 2020. (a) 2018. (b) 2019. (c) 2020.

2) Comparison With Existing Remote Sensing Products: Compared with the classification results of the two 10-m resolution remote sensing products of the ESA WorldCover 2020 and ESRI 2020 LULC, and the impervious surfaces of Wuhan in 2020 extracted in this article, the feasibility and effectiveness of the method proposed are discussed. Six local areas where the types of more complex ground objects at the junction of urban and rural areas are selected under the original remote sensing image of Sentinel-2 Level-1C production are shown in Fig. 9. The results show that the degree of refinement of the ESRI 2020 LULC is relatively low, and it has an overestimation of the impervious surfaces in case of the pervious surfaces exist in the impervious surface area. For the ESA WorldCover 2020, the road boundaries of houses and roads with a small area can be accurately extracted with fewer missing points, but it has poor extraction of bright impervious surfaces, resulting in an underestimation of impervious surfaces. For the result in this article, it is more conducive to accurately distinguishing the boundary between impervious and pervious surfaces, the relatively obvious boundaries of houses and roads, and it also has a more refined extraction of bright impervious surfaces. The accuracy assessments of the impervious surface extraction results obtained by this article, ESA WorldCover 2020, and the ESRI 2020 LULC are shown in Fig. 10. Therefore, the impervious surface training samples extracted by the proposed method are practical.

TABLE V
ACCURACY ASSESSMENT WITH THE CONFUSION MATRIX OF CLASSIFICATION RESULTS FOR IMPERVIOUS SURFACES IN WUHAN FROM 2018 TO 2020 IN THIS ARTICLE

Year	Predicted class	Actual class: Pervious surface samples	Actual class: Impervious surface samples	Total	PA (%)
2018	Pervious surface samples	1226	65	1291	94.97
	Impervious surface samples	35	345	380	90.79
	Total	1261	410		
	UA (%)	97.22	84.15		
	OA (%)	94.02			
	Kappa coefficient	0.83			
2019	Pervious surface samples	1328	75	1403	94.65
	Impervious surface samples	15	204	219	93.15
	Total	1343	279		
	UA (%)	98.88	73.12		
	OA (%)	94.45			
	Kappa coefficient	0.79			
2020	Pervious surface samples	1327	84	1411	94.05
	Impervious surface samples	16	205	221	92.76
	Total	1343	289		
	UA (%)	98.81	70.93		
	OA (%)	93.87			
	Kappa coefficient	0.77			

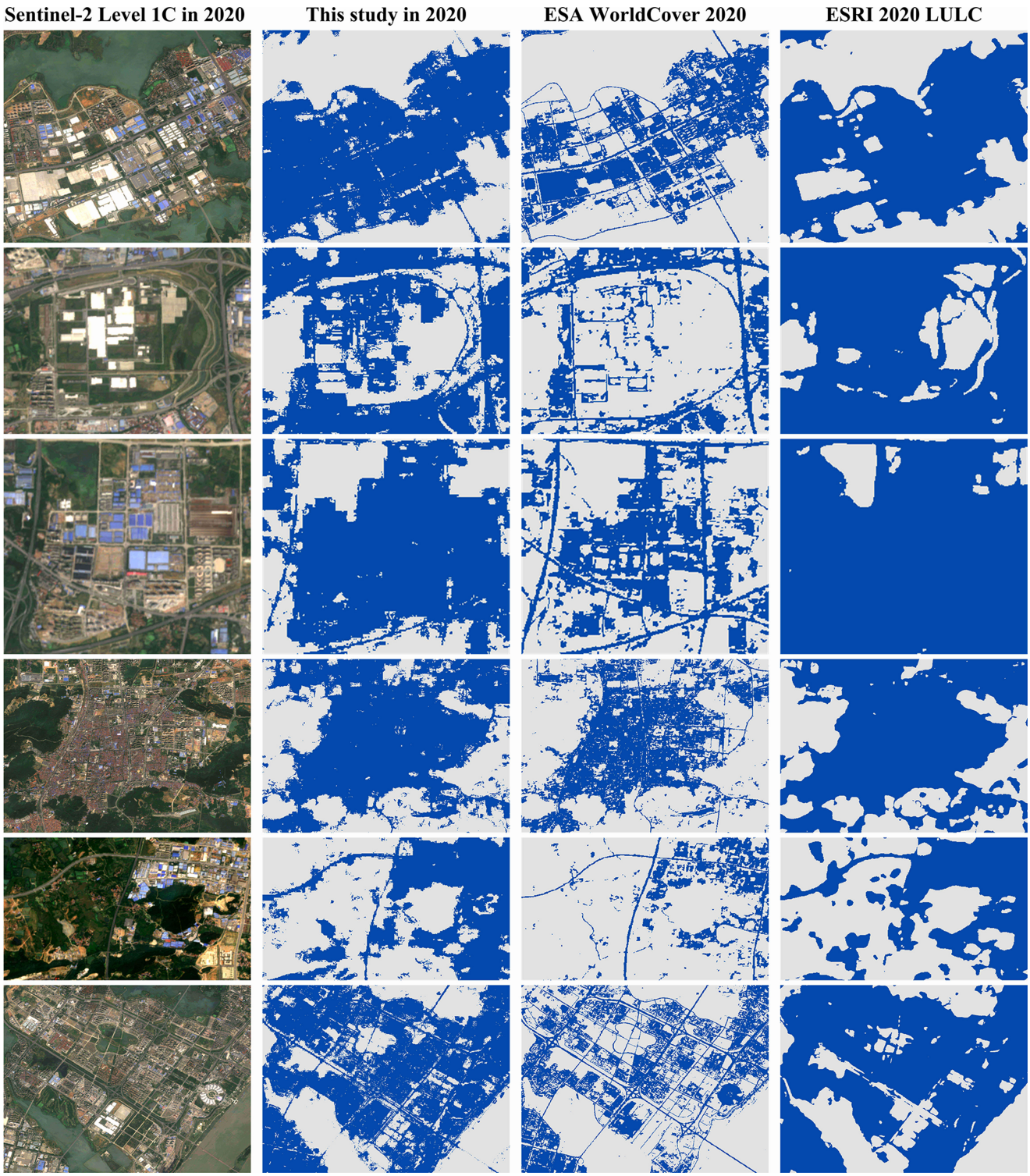

Fig. 9. Comparison of the impervious surface extraction results obtained by this article and two 10-m resolution remote sensing products of the ESA WorldCover 2020 and the ESRI 2020 LULC in six local areas of Wuhan in 2020.

B. Discussion

1) Accuracy Assessment of the Generated Training Samples: In terms of sample accuracy assessment, Olofsson et al. [78] pointed out that probability sampling design can be implemented considering actual conditions. Given that the number of sample sets is still large after sample selection and purification, this article randomly selects the same number of each feature type to improve efficiency. A total of 5000 samples of each feature type are randomly selected by the stratified random sampling method. Additionally, 5% of the stratified random samples, that

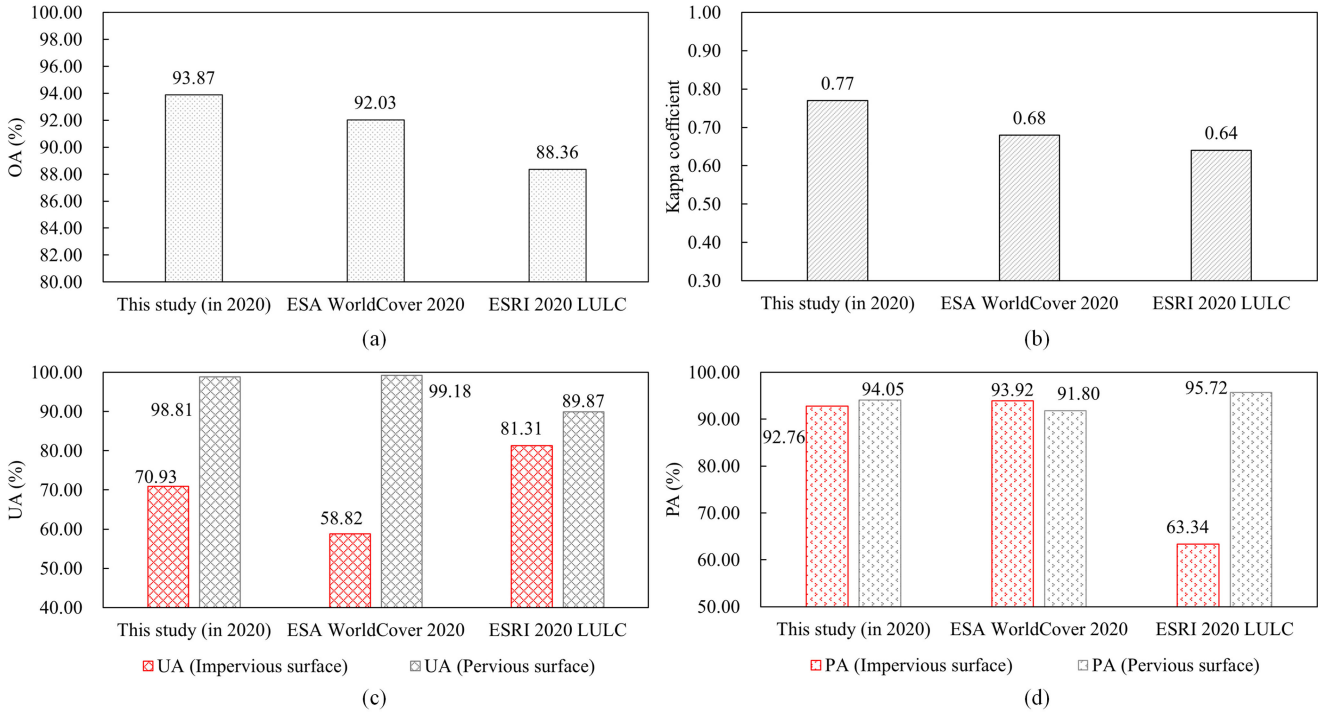

Fig. 10. Accuracy assessments of the impervious surface extraction results obtained by this article, and two remote sensing products of ESA WorldCover 2020 and the ESRI 2020 LULC. (a) OA. (b) Kappa coefficient. (c) UA. (d) PA.

TABLE VI
ACCURACY ASSESSMENT WITH THE CONFUSION MATRIX OF SIX FEATURE TYPES FOR THE STRATIFIED RANDOM SAMPLES OF WUHAN IN 2018

Predicted class	Actual class: Arable land	Woodland	Grassland	Waters	Urban and rural, residential, industrial, and mining land	Unused land	Total	PA (%)
Arable land	226	2	12	0	4	72	316	71.52
Woodland	20	246	3	0	0	4	273	90.11
Grassland	2	2	235	0	2	2	243	96.71
Waters	0	0	0	250	0	4	254	98.43
Urban and rural, residential, industrial, and mining land	0	0	0	0	242	1	243	99.59
Unused land	2	0	0	0	2	167	171	97.66
Total	250	250	250	250	250	250		
UA (%)	90.40	98.40	94.00	100.00	96.80	66.80		
OA (%)	91.07							
Kappa coefficient	0.89							

is, 250 samples of each feature type, are also randomly selected for accuracy assessment. Through visual interpretation of Sentinel-2 images, the confusion matrix [79] with OA, kappa coefficient, UA, and PA is used to evaluate the accuracy of the classification results for the training samples. The accuracy assessment results of the six feature types for the stratified random samples of Wuhan in 2018 are displayed in the confusion matrix with an OA of 91.07% (Table VI).

To evaluate the sample accuracy of the impervious surface and pervious surface, the six feature types are reclassified into two types. Among them, five feature types of arable land, woodland, grassland, waters, and unused land are regarded as pervious surfaces, and the feature type of urban and rural, residential, industrial, and mining land is regarded as impervious surfaces. The accuracy assessment results of the two types of stratified random samples of Wuhan in 2018 are displayed in the confusion matrix with an OA of 99.4% (Table VII). Therefore, it is conducive to the performance of the training samples for impervious surfaces in practical applications.

2) Sample Separability Assessment: To verify the separability of training samples for the impervious surfaces and the background pervious surfaces, both the Jeffries-Matusita (JM) distance [80] and the transformed divergence (TD) distance [81] are calculated in this article. The JM distance and the TD distance for the training samples based on remote sensing data of Wuhan in 2018 are 1.84 and 1.99, respectively. The JM distance of impervious surfaces is more than 1.8, which indicates the high separability between the impervious surfaces

TABLE VII
ACCURACY ASSESSMENT WITH THE CONFUSION MATRIX OF TWO TYPES, I.E., IMPERVIOUS SURFACES AND PERVIOUS SURFACES, FOR THE STRATIFIED RANDOM SAMPLES FOR WUHAN IN 2018

	Actual class			
Predicted class	Impervious surface samples	Pervious surface samples	Total	PA (%)
Impervious surface samples	1249	8	1257	99.36
Pervious surface samples	1	242	243	99.59
Total	1250	250		
UA (%)	99.92	96.80		
OA (%)	99.40			
Kappa coefficient	0.98			

and the background pervious surfaces, and the powerful capability of the automatically generating training sample's method for impervious surface extraction.

3) Limitations and Future Article: In this article, Sentinel-2 images are directly used as the original data, and multiple spectral indices, including NDVI, MNDWI, NDBI, and SoEI, as well as DSM elevation data, are added as auxiliary data. Only the spectral information of the composite Sentinel-2 images is used in the classification process. Next article can consider adding other features, for example, texture, to improve the efficiency and accuracy of impervious surface classification. Meanwhile, to further improve the accuracy of impervious surfaces, the next article will also consider the distinction between impervious surface types, including the bright impervious surfaces and dark impervious surfaces. In addition, the experiment in this article only conducts a case study on Wuhan city in 3 years, which verifies the feasibility of the proposed method. In the future, it will be explored in adopting other high-resolution images with longer time coverage for the long-term series analysis of impervious surfaces and improving the applicability of spectral index thresholds in different regions.

V. CONCLUSION

It is important to reduce manual participation in training sample acquisition and improve the efficiency of impervious surface extraction. The purpose of this article is to propose a method of impervious surface extraction based on automatically generating training samples from Sentinel-2 images, multisource remote sensing products of GAIA, AULM, and CNLUCC, as well as DSM data. The contributions of this article are primarily twofold: 1) a method is proposed for automatically generating training samples of impervious surfaces with 10-m resolution and improved sample quality, and 2) a powerful strategy is designed through training sample migration, which can be applied to obtain the training samples in the year with limited classification products based on the certain year with available classification products. The accuracy assessment of the training samples showed that the extracted training sample set of Wuhan in 2018 had a higher accuracy with an OA of 99.40% and kappa coefficient of 0.98 with the automatic extraction process, thus reducing repetitive manual participation. In addition, due to the time constraints of remote sensing products for impervious surfaces and land use, based on the generated training sample set, sample migration was adopted to perform change detection based on principle component analysis to obtain the respective training sample sets in 2019 and 2020. To further validate the availability of the training samples by the method proposed, the obtained training sample sets were used for random forest model training to extract the distribution of impervious surfaces of Wuhan in 2018, 2019, and 2020 with OAs of 94.02%, 94.45%, and 93.87%, respectively. The spatial resolution of the final classification result of the impervious surfaces in this article was improved from 30 m of the original remote sensing products to 10 m.

ACKNOWLEDGMENT

The authors would like to thank the following data, tool, and service providers: ESA for providing Sentinel-2 Level-1C product, Gong et al. from Tsinghua University for providing GAIA, Liu et al. from Wuhan University for providing AULM, Xu et al. from Chinese Academy of Sciences for providing CNLUCC, JAXA for providing ALOS AW3D30 version 2.1 product of global DSM, and Google for providing the GEE cloud platform.

REFERENCES

[1] C. L. Arnold and C. J. Gibbons, "Impervious surface coverage: The emergence of a key environmental indicator," *J. Amer. Plan. Assoc.*, vol. 62, no. 2, pp. 243–258, 1996, doi: 10.1080/01944369608975688.
[2] F. B. Balcik, "Determining the impact of urban components on land surface temperature of Istanbul by using remote sensing indices," *Environ. Monit. Assessment*, vol. 186, no. 2, pp. 859–872, 2014, doi: 10.1007/s10661-013-3427-5.
[3] S. E. Brun and L. E. Band, "Simulating runoff behavior in an urbanizing watershed," *Comput. Environ. Urban Syst.*, vol. 24, no. 1, pp. 5–22, 2000.
[4] D. L. Civco and J. D. Hurd, "Impervious surface mapping for the state of connecticut," *Investment Manage. Weekly*, vol. 52, no. 11, pp. 1271–1282, 1997.
[5] R. R. Gillies, J. B. Box, J. Symanzik, and E. J. Rodemaker, "Effects of urbanization on the aquatic fauna of the line creek watershed, Atlanta—A satellite perspective," *Remote Sens. Environ.*, vol. 86, no. 3, pp. 411–422, 2003, doi: 10.1016/S0034-4257(03)00082-8.
[6] U. Rajasekar and Q. H. Weng, "Urban heat island monitoring and analysis using a non-parametric model: A case study of Indianapolis," *ISPRS J. Photogramm.*, vol. 64, no. 1, pp. 86–96, 2009, doi: 10.1016/j.isprsjprs.2008.05.002.
[7] M. K. Ridd, "Exploring a V-I-S (Vegetation-Impervious surface-soil) model for urban ecosystem analysis through remote sensing," *Int. J. Remote Sens.*, vol. 16, no. 12, pp. 2165–2185, 1995.
[8] D. A. Roberts, M. Gardner, R. Church, S. Ustin, G. Scheer, and R. O. Green, "Mapping chaparral in the Santa Monica mountatins using multiple endmember spectral mixture models," *Remote Sens. Environ.*, vol. 65, no. 3, pp. 267–279, 1998.

[9] C. S. Wu and A. T. Murray, "Estimating impervious surface distribution by spectral mixture analysis," *Remote Sens. Environ.*, vol. 84, no. 4, pp. 493–505, 2003, doi: 10.1016/S0034-4257(02)00136-0.

[10] C. Liu, Z. F. Shao, M. Chen, and H. Luo, "MNDISI: A multi-source composition index for impervious surface area estimation at the individual city scale," *Remote Sens. Lett.*, vol. 4, no. 8, pp. 803–812, 2013, doi: 10.1080/2150704X.2013.798710.

[11] Z. Q. Wang, C. C. Gang, X. L. Li, Y. Z. Chen, and J. L. Li, "Application of a normalized difference impervious index (NDII) to extract urban impervious surface features based on Landsat TM images," *Int. J. Remote Sens.*, vol. 36, no. 4, pp. 1055–1069, 2015, doi: 10.1080/01431161.2015.1007250.

[12] H. Q. Xu, "Analysis of impervious surface and its impact on urban heat environment using the normalized difference impervious surface index (NDISI)," *Photogramm. Eng. Remote Sens.*, vol. 76, no. 5, pp. 557–565, 2010, doi: 10.14358/PERS.76.5.557.

[13] J. Im, Z. Y. Lu, J. Rhee, and L. J. Quackenbush, "Impervious surface quantification using a synthesis of artificial immune networks and decision/regression trees from multi-sensor data," *Remote Sens. Environ.*, vol. 117, pp. 102–113, 2012, doi: 10.1016/j.rse.2011.06.024.

[14] W. L. Li, C. S. Wu, and W. Choi, "Predicting future urban impervious surface distribution using cellular automata and regression analysis," *Earth Sci. Inform.*, vol. 11, no. 1, pp. 19–29, 2018, doi: 10.1007/s12145-017-0312-8.

[15] B. Matthias and H. Martin, "Mapping imperviousness using NDVI and linear spectral unmixing of ASTER data in the Cologne-Bonn region (Germany)," in *Proc. Remote Sens. Environ. Monit., GIS Appl., Geol. III*, 2004, pp. 274–284.

[16] D. Y. Hu, S. S. Chen, K. Qiao, and S. S. Cao, "Integrating CART algorithm and multi-source remote sensing data to estimate sub-pixel impervious surface coverage: A case study from Beijing municipality, China," *Chin. Geogr. Sci.*, vol. 27, no. 4, pp. 614–625, 2017, doi: 10.1007/s11769-017-0882-x.

[17] J. R. Parent, J. C. Volin, and D. L. Civco, "A fully-automated approach to land cover mapping with airborne LiDAR and high resolution multispectral imagery in a forested suburban landscape," *ISPRS J. Photogramm.*, vol. 104, pp. 18–29, 2015, doi: 10.1016/j.isprsjprs.2015.02.012.

[18] J. H. Bian, A. N. Li, J. Q. Zuo, G. B. Lei, Z. J. Zhang, and X. Nan, "Estimating 2009–2017 impervious surface change in Gwadar, Pakistan using the HJ-1A/B constellation, GF-1/2 data, and the random forest algorithm," *ISPRS Int. Geo-Inf.*, vol. 8, no. 10, 2019, Art. no. 443, doi: 10.3390/ijgi8100443.

[19] X. G. Dong, Z. G. Meng, Y. Z. Wang, Y. Z. Zhang, H. T. Sun, and Q. S. Wang, "Monitoring spatiotemporal changes of impervious surfaces in Beijing city using random forest algorithm and textural features," *Remote Sens.*, vol. 13, no. 1, 2021, Art. no. 153, doi: 10.3390/rs13010153.

[20] Z. F. Shao, H. Y. Fu, P. Fu, and L. Yin, "Mapping urban impervious surface by fusing optical and SAR data at the decision level," *Remote Sens.*, vol. 8, no. 11, 2016, Art. no. 945, doi: 10.3390/rs8110945.

[21] B. Shrestha, H. Stephen, and S. Ahmad, "Impervious surfaces mapping at city scale by fusion of radar and optical data through a random forest classifier," *Remote Sens.*, vol. 13, no. 15, 2021, Art. no. 3040, doi: 10.3390/rs13153040.

[22] F. H. Huang, Y. Yu, and T. H. Feng, "Automatic extraction of urban impervious surfaces based on deep learning and multi-source remote sensing data," *J. Vis. Commun. Image Representation*, vol. 60, pp. 16–27, 2019, doi: 10.1016/j.jvcir.2018.12.051.

[23] J. R. Parekh, A. Poortinga, B. Bhandari, T. Mayer, D. Saah, and F. Chishtie, "Automatic detection of impervious surfaces from remotely sensed data using deep learning," *Remote Sens.*, vol. 13, no. 16, 2021, Art. no. 3166, doi: 10.3390/rs13163166.

[24] Y. Y. Xu, L. Wu, Z. Xie, and Z. L. Chen, "Building extraction in very high resolution remote sensing imagery using deep learning and guided filters," *Remote Sens.*, vol. 10, no. 1, 2018, Art. no. 144, doi: 10.3390/rs10010144.

[25] R. Y. Yin et al., "Automatic framework of mapping impervious surface growth with long-term Landsat imagery based on temporal deep learning model," *IEEE Geosci. Remote Sens. Lett.*, vol. 19, Jan. 2022, Art. no. 2502605, doi: 10.1109/LGRS.2021.3135869.

[26] J. Plaza, C.-I. Chang, A. Plaza, R. Perez, and P. Martinez, "On the generation of training samples for neural network-based mixed pixel classification," in *Proc. Algorithms Technol. Multispectral, Hyperspectral, Ultraspectral Imagery XI*, 2005, pp. 149–160, doi: 10.1117/12.604114.

[27] X. Capron, B. Walczak, O. E. de Noord, and D. L. Massart, "Selection and weighting of samples in multivariate regression model updating," *Chemometrics Intell. Lab. Syst.*, vol. 76, no. 2, pp. 205–214, 2005, doi: 10.1016/j.chemolab.2004.11.003.

[28] N. Chen, M. L. Zhu, Y. Jiang, and A. Chen, "The relationship between decision trees and the scale of train data set," in *Proc. 6th World Congr. Intell. Control Autom.*, 2006, pp. 6087–6091.

[29] L. Breiman, "Random forests," *Mach. Learn.*, vol. 45, no. 1, pp. 5–32, 2001, doi: 10.1023/A:1010933404324.

[30] T. K. Ho, "Random decision forests," in *Proc. 3rd Int. Conf. Document Anal. Recognit.*, 1995, pp. 278–282.

[31] M. Belgiu and L. Dragut, "Random forest in remote sensing: A review of applications and future directions," *ISPRS J. Photogramm.*, vol. 114, pp. 24–31, 2016, doi: 10.1016/j.isprsjprs.2016.01.011.

[32] Z. Z. Chen, M. Huang, D. Y. Zhu, and O. Altan, "Integrating remote sensing and a Markov-FLUS model to simulate future land use changes in Hokkaido, Japan," *Remote Sens.*, vol. 13, no. 13, 2021, Art. no. 2621, doi: 10.3390/rs13132621.

[33] Z. Jiang, X. Zhu, W.-T. Tan, and R. Liston, "Training sample selection for deep learning of distributed data," in *Proc. IEEE Int. Conf. Image Process.*, 2017, pp. 2189–2193.

[34] Z. Lv, G. Li, J. Yan, J. A. Benediktsson, and Z. You, "Training samples enriching approach for classification improvement of VHR remote sensing image," *IEEE Geosci. Remote Sens. Lett.*, vol. 19, Dec. 2021, Art. no. 6002405, doi: 10.1109/LGRS.2021.3067927.

[35] M. Huang, N. C. Chen, W. Y. Du, Z. Q. Chen, and J. Y. Gong, "DMBLC: An indirect urban impervious surface area extraction approach by detecting and masking background land cover on Google earth image," *Remote Sens.*, vol. 10, no. 5, 2018, Art. no. 766, doi: 10.3390/rs10050766.

[36] H. N. Guo, Q. Shi, A. Marinoni, B. Du, and L. P. Zhang, "Deep building footprint update network: A semi-supervised method for updating existing building footprint from bi-temporal remote sensing images," *Remote Sens. Environ.*, vol. 264, 2021, Art. no. 112589, doi: 10.1016/j.rse.2021.112589.

[37] A. K. Piyoosh and S. K. Ghosh, "Semi-automatic mapping of anthropogenic impervious surfaces in an urban/suburban area using Landsat 8 satellite data," *GIsci. Remote Sens.*, vol. 54, no. 4, pp. 471–494, 2017, doi: 10.1080/15481603.2017.1282414.

[38] H. Zhang, S. M. Gorelick, and P. V. Zimba, "Extracting impervious surface from aerial imagery using semi-automatic sampling and spectral stability," *Remote Sens.*, vol. 12, no. 3, 2020, Art. no. 506, doi: 10.3390/rs12030506.

[39] Y. Wang and M. Li, "Urban impervious surface automatic threshold detection model derived from multitemporal Landsat images," *IEEE Trans. Geosci. Remote Sens.*, vol. 60, Jan. 2022, Art. no. 4503321, doi: 10.1109/TGRS.2021.3089581.

[40] K. Tan, X. Jin, A. Plaza, X. S. Wang, L. Xiao, and P. J. Du, "Automatic change detection in high-resolution remote sensing images by using a multiple classifier system and spectral-spatial features," *IEEE J. Sel. Topics Appl. Earth Observ. Remote Sens.*, vol. 9, no. 8, pp. 3439–3451, Aug. 2016, doi: 10.1109/JSTARS.2016.2541678.

[41] B. Hou, Y. H. Wang, and Q. J. Liu, "A saliency guided semi-supervised building change detection method for high resolution remote sensing images," *Sensors*, vol. 16, no. 9, 2016, Art. no. 1377, doi: 10.3390/s16091377.

[42] Y. X. Zhou, Y. Song, S. X. Cui, H. T. Zhu, J. Sun, and W. J. Qin, "A novel change detection framework in urban area using multilevel matching feature and automatic sample extraction strategy," *IEEE J. Sel. Topics Appl. Earth Observ. Remote Sens.*, vol. 14, pp. 3967–3987, Apr. 2021, doi: 10.1109/JSTARS.2021.3064311.

[43] I. Sebari and D. C. He, "Automatic fuzzy object-based analysis of VHSR images for urban objects extraction," *ISPRS J. Photogramm.*, vol. 79, pp. 171–184, 2013, doi: 10.1016/j.isprsjprs.2013.02.006.

[44] C. Liu, X. Huang, Z. Zhu, H. J. Chen, X. M. Tang, and J. Y. Gong, "Automatic extraction of built-up area from ZY3 multi-view satellite imagery: Analysis of 45 global cities," *Remote Sens. Environ.*, vol. 226, pp. 51–73, 2019, doi: 10.1016/j.rse.2019.03.033.

[45] M. Huang, N. C. Chen, W. Y. Du, M. T. Wen, D. Y. Zhu, and J. Y. Gong, "An on-demand scheme driven by the knowledge of geospatial distribution for large-scale high-resolution impervious surface mapping," *GISci. Remote Sens.*, vol. 58, no. 4, pp. 562–586, 2021, doi: 10.1080/15481603.2021.1909304.

[46] A. Schneider, M. A. Friedl, and D. Potere, "Mapping global urban areas using MODIS 500-m data: New methods and datasets based on 'urban ecoregions'," *Remote Sens. Environ.*, vol. 114, no. 8, pp. 1733–1746, 2010, doi: 10.1016/j.rse.2010.03.003.
[47] "A consistent 300 m global land cover and land cover change time series from 1992 to 2015 derived from multi-mission reprocessed archives," Land Cover Component of ESA Climate Change Initiative, 2016, Accessed: Dec. 6, 2021. [Online]. Available: http://www.gofcgold.wur.nl/documents/Sciencemeeting2016/GLCM/PDefourny1.pdf
[48] "GHS-BUILT R2018A," European Commission, 2018, Accessed: Dec. 6, 2021. [Online]. Available: https://ghsl.jrc.ec.europa.eu/ghs_bu2019.php
[49] P. Gong, X. C. Li, and W. Zhang, "40-year (1978–2017) human settlement changes in China reflected by impervious surfaces from satellite remote sensing," *Sci. Bull.*, vol. 64, no. 11, pp. 756–763, 2019, doi: 10.1016/j.scib.2019.04.024.
[50] P. Gong et al., "Finer resolution observation and monitoring of global land cover: First mapping results with Landsat TM and ETM+ data," *Int. J. Remote Sens.*, vol. 34, no. 7, pp. 2607–2654, 2013, doi: 10.1080/01431161.2012.748992.
[51] X. P. Liu et al., "High-spatiotemporal-resolution mapping of global urban change from 1985 to 2015," *Nature Sustain.*, vol. 3, no. 7, pp. 564–570, 2020, doi: 10.1038/s41893-020-0521-x.
[52] X. Liu et al., "High-resolution multi-temporal mapping of global urban land using Landsat images based on the Google Earth Engine platform," *Remote Sens. Environ.*, vol. 209, pp. 227–239, 2018, doi: https://doi.org/10.1016/j.rse.2018.02.055.
[53] J. Chen et al., "Spatial distribution and ten years change of global built-up areas derived from globeland30," *Acta Geodaetica et Cartographica Sinica*, vol. 44, no. 11, pp. 1181–1188, 2015.
[54] J. Yang and X. Huang, "The 30 m annual land cover dataset and its dynamics in China from 1990 to 2019," *Earth Syst. Sci. Data*, vol. 13, no. 8, pp. 3907–3925, 2021, doi: 10.5194/essd-13-3907-2021.
[55] K. Karra, C. Kontgis, Z. Statman-Weil, J. C. Mazzariello, M. Mathis, and S. P. Brumby, "Global land use/land cover with sentinel 2 and deep learning," in *Proc. IEEE Int. Geosci. Remote Sens. Symp.*, 2021, pp. 4704–4707, doi: 10.1109/IGARSS47720.2021.9553499.
[56] "Sentinel-2 10m land use/land cover timeseries downloader," ESRI, 2021. Accessed: Jan. 8, 2022. [Online]. Available: https://www.arcgis.com/apps/instant/media/index.html?appid=fc92d38533d440078f17678ebc20e8e2
[57] "*Worldwide land cover mapping*," ESA, 2020. Accessed: Jan. 8, 2022. [Online]. Available: https://esa-worldcover.org/en
[58] Z. Shao, Y. Zhang, X. Huang, X. Zhu, L. Wu, and B. Wan, "Mapping impervious surface with 2 m using multi-source high resolution remote sensing images," *Geomatics Inf. Sci. Wuhan Univ.*, vol. 43, no. 12, pp. 1909–1915, 2018, doi: 10.13203/j.whugis20180196.
[59] G. Xian and M. Crane, "Assessments of urban growth in the Tampa Bay watershed using remote sensing data," *Remote Sens. Environ.*, vol. 97, no. 2, pp. 203–215, 2005, doi: 10.1016/j.rse.2005.04.017.
[60] L. M. Yang, C. Q. Huang, C. G. Homer, B. K. Wylie, and M. J. Coan, "An approach for mapping large-area impervious surfaces: Synergistic use of Landsat-7 ETM+ and high spatial resolution imagery," *Can. J. Remote Sens.*, vol. 29, no. 2, pp. 230–240, 2003, doi: 10.5589/m02-098.
[61] L. Zhang and Q. H. Weng, "Annual dynamics of impervious surface in the pearl river delta, China, from 1988 to 2013, using time series Landsat imagery," *ISPRS J. Photogramm.*, vol. 113, pp. 86–96, 2016, doi: 10.1016/j.isprsjprs.2016.01.003.
[62] "China's multi-period land use land cover remote sensing monitoring data set (CNLUCC)," Chinese Academy of Sciences, 2018. Accessed: Dec. 6, 2021. [Online]. Available: https://www.resdc.cn/data.aspx?DATAID=264
[63] "Sentinel-2 level-1C," European Space Agency, 2021. Accessed: Jan. 8, 2022. [Online]. Available: https://scihub.copernicus.eu/dhus/#/home
[64] P. Gong et al., "Annual maps of global artificial impervious area (GAIA) between 1985 and 2018," *Remote Sens. Environ.*, vol. 236, 2020, Art. no. 111510, doi: 10.1016/j.rse.2019.111510.
[65] P. Gong et al., "Stable classification with limited sample: Transferring a 30-m resolution sample set collected in 2015 to mapping 10-m resolution global land cover in 2017," *Sci. Bull.*, vol. 64, no. 6, pp. 370–373, 2019, doi: 10.1016/j.scib.2019.03.002.
[66] X. C. Li and P. Gong, "An 'exclusion-inclusion' framework for extracting human settlements in rapidly developing regions of China from Landsat images," *Remote Sens. Environ.*, vol. 186, pp. 286–296, 2016, doi: 10.1016/j.rse.2016.08.029.
[67] "GAIA file list," Tsinghua University, 2018. Accessed: Dec. 6, 2021. [Online]. Available: http://data.ess.tsinghua.edu.cn/gaia.html
[68] D. D. Liu, N. C. Chen, X. Zhang, C. Wang, and W. Y. Du, "Annual large-scale urban land mapping based on Landsat time series in Google Earth Engine and openstreetmap data: A case study in the middle Yangtze river basin," *ISPRS J. Photogramm.*, vol. 159, pp. 337–351, 2020, doi: 10.1016/j.isprsjprs.2019.11.021.
[69] "ALOS global digital surface model 'ALOS world 3D - 30m' (AW3D30)," Earth Observations Research Center, 2018. [Online]. Available: https://www.eorc.jaxa.jp/ALOS/en/aw3d30/registration.htm
[70] C. J. Tucker, "Red and photographic infrared linear combinations for monitoring vegetation," *Remote Sens. Environ.*, vol. 8, no. 2, pp. 127–150, 1979, doi: 10.1016/0034-4257(79)90013-0.
[71] H. Q. Xu, "Modification of normalised difference water index (NDWI) to enhance open water features in remotely sensed imagery," *Int. J. Remote Sens.*, vol. 27, no. 14, pp. 3025–3033, 2006, doi: 10.1080/01431160600589179.
[72] Y. Zha, J. Gao, and S. Ni, "Use of normalized difference built-up index in automatically mapping urban areas from TM imagery," *Int. J. Remote Sens.*, vol. 24, no. 3, pp. 583–594, 2003, doi: 10.1080/01431160304987.
[73] G. L. Feyisa, H. Meilby, G. D. Jenerette, and S. Pauliet, "Locally optimized separability enhancement indices for urban land cover mapping: Exploring thermal environmental consequences of rapid urbanization in Addis Ababa, Ethiopia," *Remote Sens. Environ.*, vol. 175, pp. 14–31, 2016, doi: 10.1016/j.rse.2015.12.026.
[74] "Block statistics," Environ. Sen. Res. Inst., 2021. Accessed: Jan. 8, 2022. [Online]. Available: https://desktop.arcgis.com/en/arcmap/latest/tools/spatial-analyst-toolbox/block-statistics.htm
[75] Q. Tao, "Study of a nonlinear mixing spectral model and some problems of vegetation classification using hyperspectral remote sensing," M.S. thesis, College Geo-Inf. Sci. Eng., Shandong Univ. Sci. Technol., Qingdao, China, 2004.
[76] Q. Tao, L. Zhang, and H. Li, "The methods for selecting training samples in vegetation classification based on hyperspectral remote sensing," *Remote Sens. Land Resour.*, vol. 64, no. 02, pp. 33–35, 2005.
[77] J. Wu and X. Yang, "Purification of training samples in supervised classification of remote sensing data," *Remote Sens. Land Resour.*, vol. 27, no. 1, pp. 36–41, 1996.
[78] P. Olofsson, G. M. Foody, M. Herold, S. V. Stehman, C. E. Woodcock, and M. A. Wulder, "Good practices for estimating area and assessing accuracy of land change," *Remote Sens. Environ.*, vol. 148, pp. 42–57, 2014, doi: 10.1016/j.rse.2014.02.015.
[79] G. M. Foody, "Status of land cover classification accuracy assessment," *Remote Sens. Environ.*, vol. 80, no. 1, pp. 185–201, 2002, doi: 10.1016/S0034-4257(01)00295-4.
[80] L. Bruzzone, F. Roli, and S. B. Serpico, "An extension of the Jeffreys-Matusita distance to multiclass cases for feature selection," *IEEE Trans. Geosci. Remote Sens.*, vol. 33, no. 6, pp. 1318–1321, Nov. 1995, doi: 10.1109/36.477187.
[81] J. A. Richards and X. Jia, *Remote Sensing Digital Image Analysis: An Introduction*, 4th ed. Berlin, Germany: Springer, 2006.

Yingbing Liu received the B.Sc. degree in geographic information system from the North China University of Water Resources and Electric Power, Zhengzhou, China, in 2014, and the Ph.D. degree in cartography and geographic information systems from the Wuhan University, Wuhan, China, in 2021.

She is currently a Lecturer with the School of Computer Science and Technology, Hainan University, Haikou, China. Her research interests include big data mining, deep learning, geospatial sensor web, and smart city.

Yuqin Wu received the B.Sc. degree in geographic information science from the Lanzhou University, Lanzhou, China, in 2019, and the M.Eng. degree in surveying and mapping engineering from the Wuhan University, Wuhan, China, in 2021.

She is currently an Engineer with the Zhongnan Engineering Corpopation Limited, Power China, Changsha, China. Her research interests include remote sensing image classification, random forest, and smart city.

Zeqiang Chen received the M.Sc. and Ph.D. degrees in cartography and geography information system from the Wuhan University, Wuhan, China, in 2008 and 2012, respectively.

He is currently a Professor with the National Engineering Research Center for Geographic Information System, China University of Geosciences, Wuhan, China. His research interests include geospatial big data, geospatial sensor web, spatiotemporal deep learning, and smart city.

Min Huang received the B.Sc. degree in remote sensing science and technology, and the Ph.D. degree in cartography and geographical information system from the Wuhan University, Wuhan, China, in 2015 and 2021, respectively.

He is currently a Lecturer with the School of Geography and Environment, Jiangxi Normal University, Nanchang, China. His research interests include urban remote sensing, smart cities, land use/land cover classification, surface parameter inversion, multi-sourced data fusion, and geospatial big data analysis.

Wenying Du received the B.Sc. degree in geographic information system from the North China University of Water Resources and Electric Power, Zhengzhou, China, in 2011, and the Ph.D. degree in photogrammetry and remote sensing from the Wuhan University, Wuhan, China, in 2017.

She is currently an Associate Professor with the National Engineering Research Center for Geographic Information System, China University of Geosciences, Wuhan, China. Her research interests include urban waterlogging, water boundary extraction, flood detection, smart city, and sensor web.

Nengcheng Chen received the B.Sc. degree in geodesy from the Wuhan Technical University of Surveying and Mapping, Wuhan, China, in 1997, and the M.S. degree in geographical information system (GIS) and the Ph.D. degree in photogrammetry and remote sensing from the Wuhan University, Wuhan, China, in 2000 and 2003, respectively.

From 2006 to 2008, he was a Postdoctoral Research Associate with the Center for Spatial Information Science and Systems, George Mason University, Fairfax, VA, USA. From 2008 to 2021, he served as a Full Professor with the State Key Laboratory of Information Engineering in Surveying, Mapping and Remote Sensing, Wuhan University, where he led the Smart Earth Team. In 2021, he was invited to be the Director of the National Engineering Research Center for Geographic Information System, also the Full Professor with the China University of Geosciences, Wuhan. He has authored and coauthored 3 books and more than 200 research papers. He was also a Leading Author of the technical report of integrated management for smart sustainable city in ITU-T FG-SSC. His research interests include sensor web, big data, real-time GIS, and smart city.

Prof. Chen was the Chair of the 2010 CPGIS Young Scholar Summer Workshop. He is a member of the International Association of Chinese Professionals in Geographic Information Sciences.

Changjiang Xiao received the B.Sc. degree in spatial-informatics & digitalized technology, and the Ph.D. degree in photogrammetry and remote sensing from the Wuhan University, China, in 2013 and 2019, respectively.

He was a Visiting Researcher with the CyberGIS Center for Advanced Digital and Spatial Studies that is hosted at the National Center for Supercomputing Applications, University of Illinois at Urbana-Champaign, Champaign, IL, USA, from 2017 to 2018. He is currently a Postdoctoral Researcher with the College of Surveying and Geo-Informatics, Tongji University, Shanghai, China. His research interests include geospatial big data analysis, geospatial sensor web, and spatiotemporal deep learning.